Supplementary Information (SI) for Lab on a Chip.
This journal is © The Royal Society of Chemistry 2026

Supplementary Figures

Modular Microfluidic Probe for Addressable Fluidic Landscapes

Ayoub Glia[1,2], Muhammedin Deliorman[1], and Mohammad A. Qasaimeh[1,2,3,4,5,*]

[1] Engineering Division, New York University Abu Dhabi, Abu Dhabi, UAE
[2] Research Center for Translational Medical Devices, New York University Abu Dhabi, Abu Dhabi, UAE
[3] Department of Mechanical and Aerospace Engineering, New York University, Brooklyn, 10003 NY, USA
[4] Department of Biomedical Engineering, New York University, Brooklyn, 10003 NY, USA
[5] NYU-KAIST Global Innovation and Research Institute, New York University, Brooklyn, 11201 NY, USA

[*] Corresponding Author, E-mail: mohammad.qasaimeh@nyu.edu

Supplementary Figures

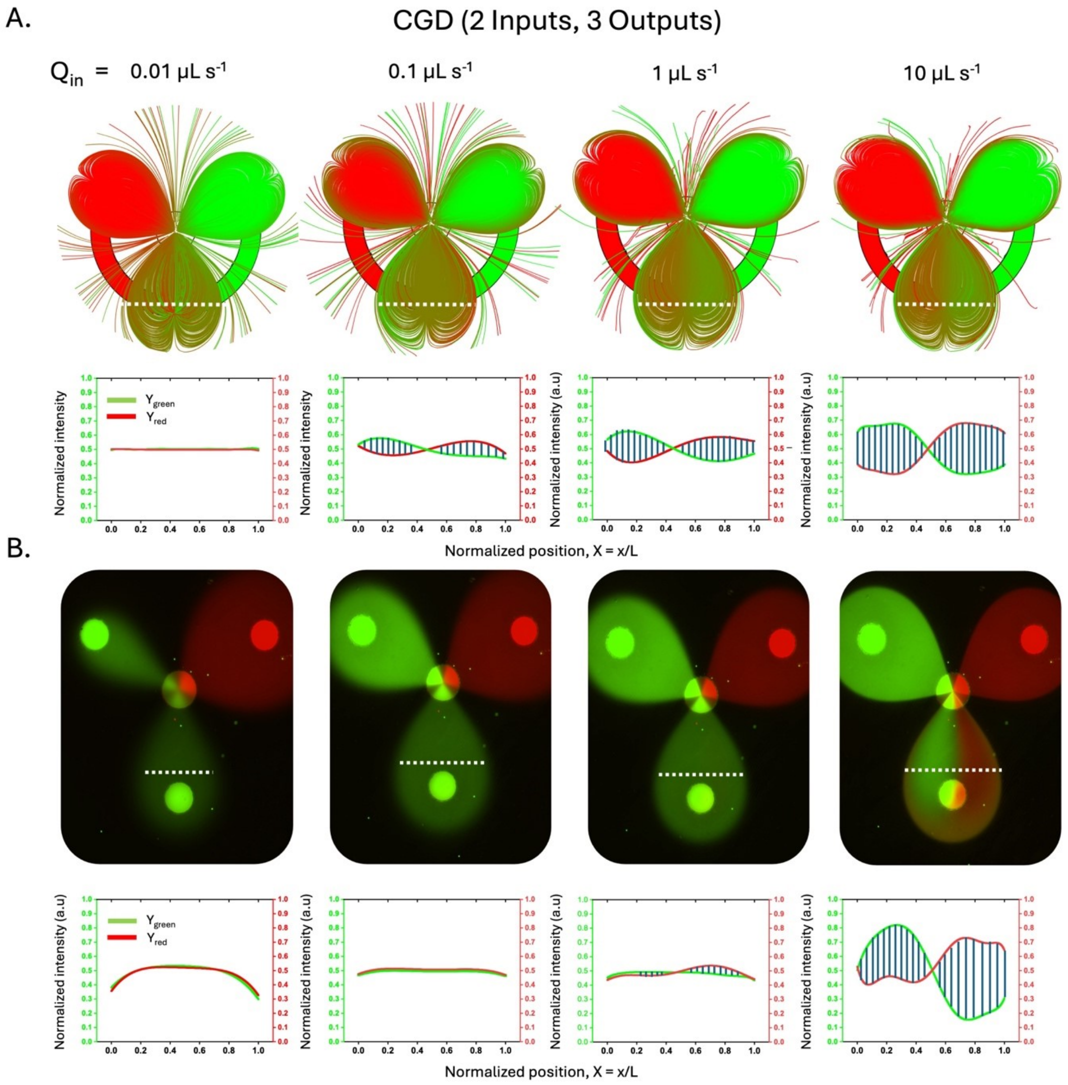

Fig. S1 Quantitative evaluation of mixing within a representative CGD output node. **(A)** Numerical simulations of the CGD (2 inputs, 3 outputs) configuration at increasing injection flow rates of $Q_{in} = 0.01\ \mu L\ s^{-1}$, $0.1\ \mu L\ s^{-1}$, $1\ \mu L\ s^{-1}$, and $10\ \mu L\ s^{-1}$ with a constant aspiration-to-injection flow-rate ratio of $\alpha = 2$. The dashed white line marks the cross-section used for profile extraction. The corresponding normalized red and green intensity profiles are shown below each panel, illustrating the transition from near-complete mixing at low flow rate to increasingly separated concentration fields at higher flow rates. **(B)** Experimental fluorescence images of the same CGD (2 inputs, 3 outputs) configuration under the corresponding flow conditions, using green and red fluorescent dyes to visualize the confined output node patterns. Dashed white lines indicate the extracted cross-sections, and the corresponding normalized intensity profiles are shown below each image. The overall agreement between (A) and (B) confirms that the numerical model captures the main flow-dependent mixing behavior observed experimentally within the representative output node.

Supplementary Figures

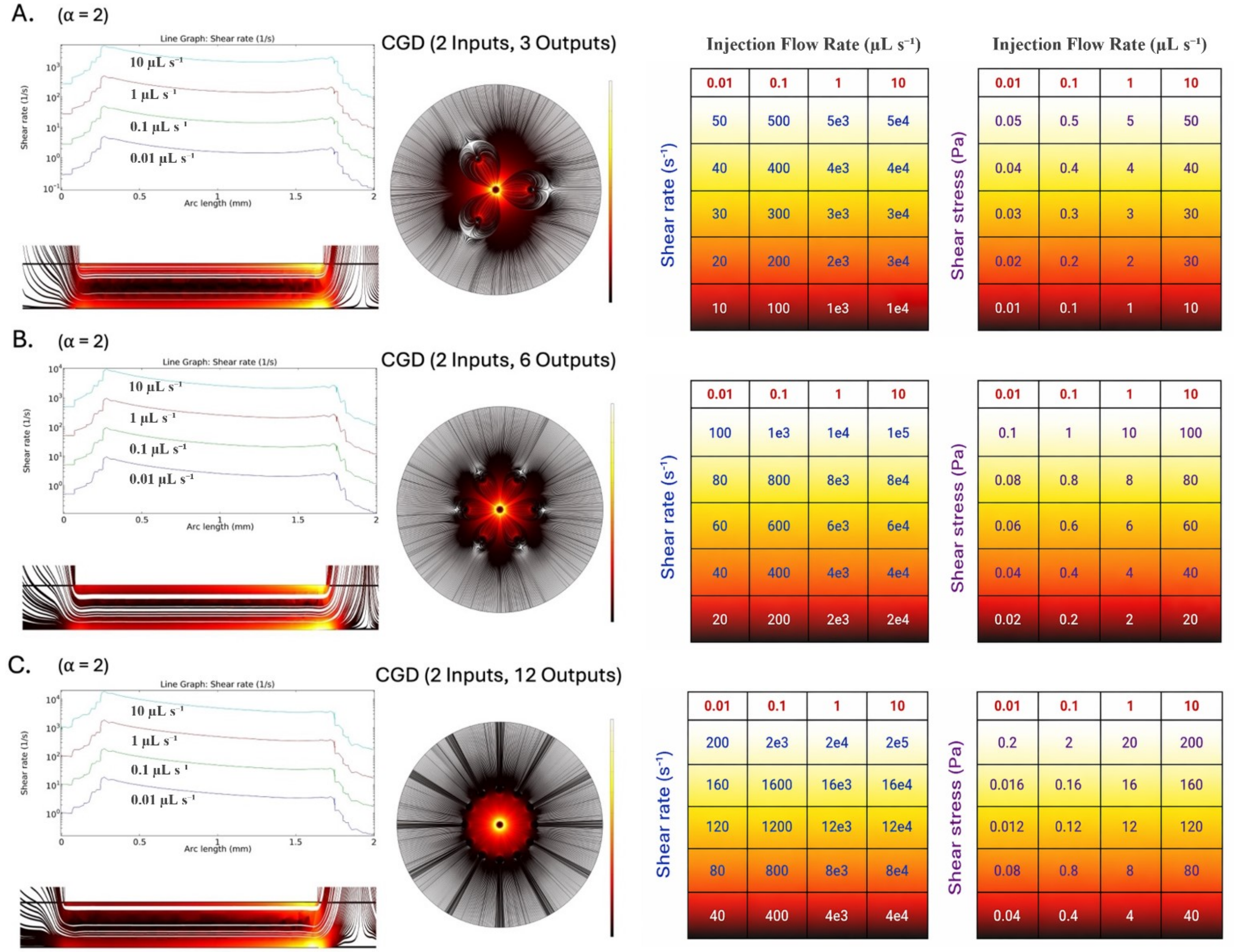

A. (α = 2) CGD (2 Inputs, 3 Outputs)

Injection Flow Rate ($\mu L\ s^{-1}$) — Shear rate (s^{-1})

0.01	0.1	1	10
50	500	5e3	5e4
40	400	4e3	4e4
30	300	3e3	3e4
20	200	2e3	3e4
10	100	1e3	1e4

Injection Flow Rate ($\mu L\ s^{-1}$) — Shear stress (Pa)

0.01	0.1	1	10
0.05	0.5	5	50
0.04	0.4	4	40
0.03	0.3	3	30
0.02	0.2	2	30
0.01	0.1	1	10

B. (α = 2) CGD (2 Inputs, 6 Outputs)

Shear rate (s^{-1})

0.01	0.1	1	10
100	1e3	1e4	1e5
80	800	8e3	8e4
60	600	6e3	6e4
40	400	4e3	4e4
20	200	2e3	2e4

Shear stress (Pa)

0.01	0.1	1	10
0.1	1	10	100
0.08	0.8	8	80
0.06	0.6	6	60
0.04	0.4	4	40
0.02	0.2	2	20

C. (α = 2) CGD (2 Inputs, 12 Outputs)

Shear rate (s^{-1})

0.01	0.1	1	10
200	2e3	2e4	2e5
160	1600	16e3	16e4
120	1200	12e3	12e4
80	800	8e3	8e4
40	400	4e3	4e4

Shear stress (Pa)

0.01	0.1	1	10
0.2	2	20	200
0.016	0.16	16	160
0.012	0.12	12	120
0.08	0.8	8	80
0.04	0.4	4	40

Fig. S2 Numerical characterization of shear conditions across CGD architectures. **(A–C)** Shear-rate and shear-stress distributions calculated for CGD (2 inputs, 3 outputs), CGD (2 inputs, 6 outputs), and CGD (2 inputs, 12 outputs) configurations, respectively, at a constant aspiration-to-injection flow-rate ratio of α = 2 and a probe-to-substrate separation distance of 100 μm. For each configuration, the left panels show the shear-rate profile extracted along the arc length of the HFC footprint (top) and a side-view cross-section of the confined region (bottom), while the center panels show the corresponding top-view streamline and shear-rate distribution within the HFC. The right panels summarize the calculated shear rate (s^{-1}) and corresponding shear stress (Pa) for injection flow rates of Q_{in} = 0.01, 0.1, 1, and 10 μL s^{-1}, assuming water-like viscosities. Across all configurations, the highest shear occurs near the aspiration apertures, whereas most of the confined processing area remains within substantially lower shear ranges.

Supplementary Figures

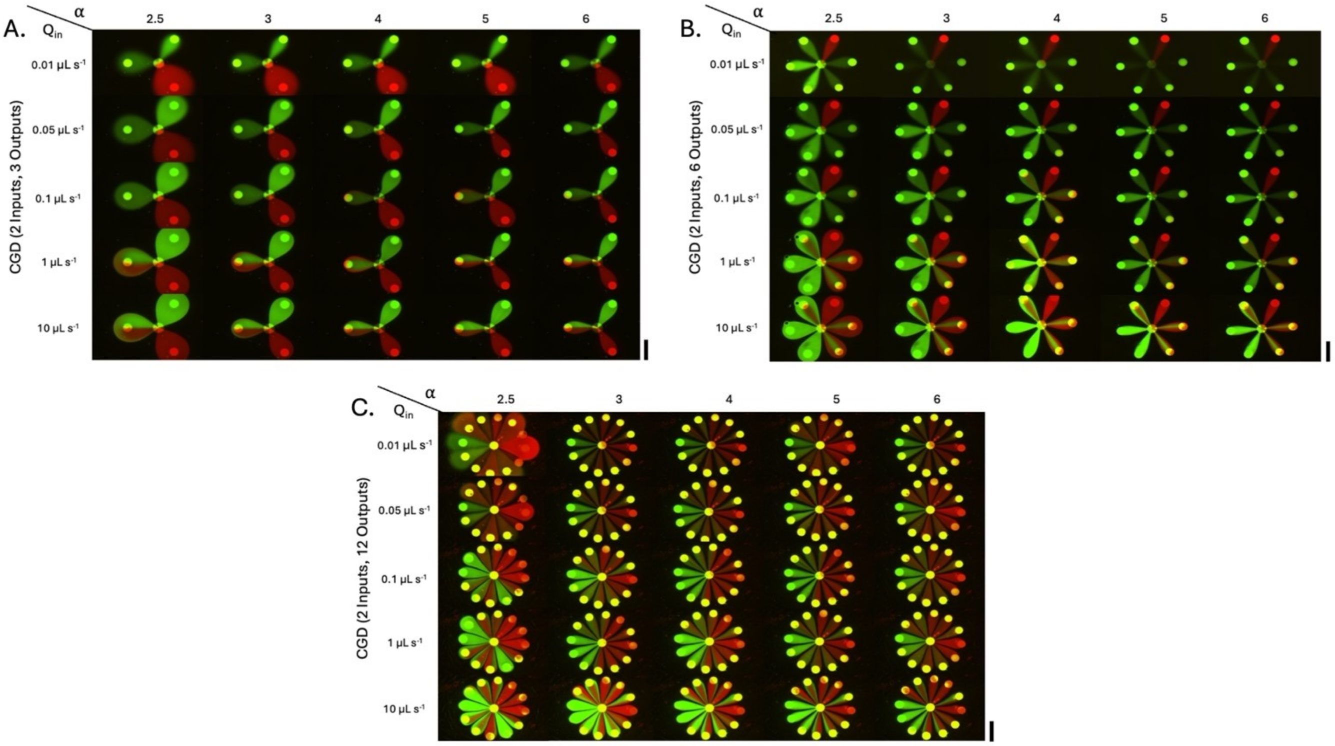

Fig. S3 Parametric characterization of CGD output patterns across flow rate and aspiration-to-injection flow-rate ratio. Representative fluorescence images showing the effect of the aspiration-to-injection flow-rate ratio ($\alpha = 2.5$, 3, 4, 5, and 6) and injection flow rate ($Q_{in} = 0.01$, 0.05, 0.1, 1, and 10 µL s^{-1}) on the output node patterns of **(A)** CGD (2 inputs, 3 outputs), **(B)** CGD (2 inputs, 6 outputs), and **(C)** CGD (2 inputs, 12 outputs). The explored parameter space defines the practical operating envelope used to assess hydrodynamic flow confinement, mixing behavior, and discretization across the different architectures. Lower flow rates favor more mixed or near-homogeneous output states, whereas higher flow rates promote increasingly discretized and spatially separated output nodes. The figure also includes boundary cases to illustrate the limits of operation, including incomplete mixing at high flow and reduced confinement sharpness at very low flow. Simpler configurations achieve clear discretization over a broader operating range, while the 2 inputs, 12 outputs design requires higher flow and shows greater sensitivity to operating conditions. Scale bars: 1 mm.

Supplementary Figures

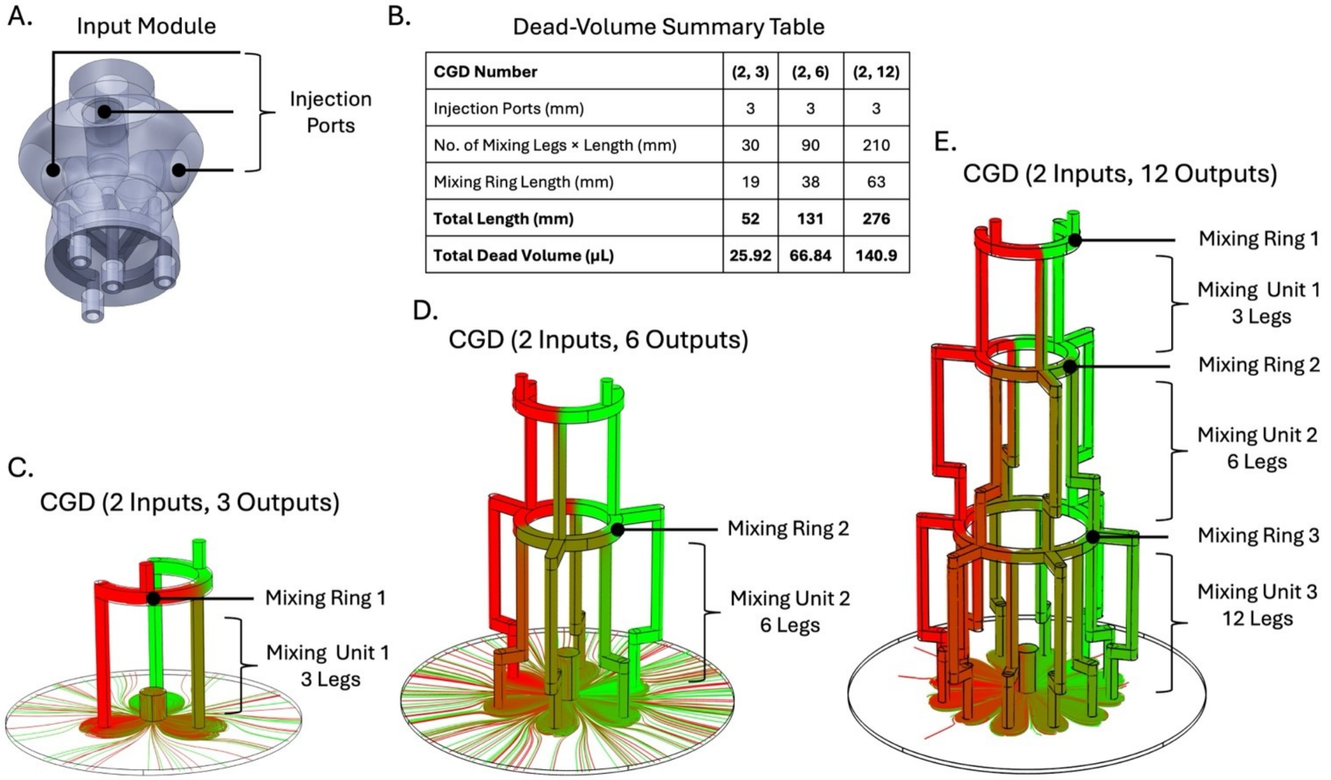

Dead-Volume Summary Table

CGD Number	**(2, 3)**	**(2, 6)**	**(2, 12)**
Injection Ports (mm)	3	3	3
No. of Mixing Legs × Length (mm)	30	90	210
Mixing Ring Length (mm)	19	38	63
Total Length (mm)	**52**	**131**	**276**
Total Dead Volume (µL)	**25.92**	**66.84**	**140.9**

Fig. S4 Architecture-dependent channel length and dead-volume scaling in CGD configurations. **(A)** Schematic of the Input module, highlighting the three injection ports that feed the downstream CGD architectures. **(B)** Dead-volume summary table for the CGD (2 inputs, 3 outputs), CGD (2 inputs, 6 outputs), and CGD (2 inputs, 12 outputs) designs, listing the number and length of mixing legs, mixing-ring length, total channel length, and estimated total dead volume. **(C–E)** Representative schematics of the CGD (2 inputs, 3 outputs), CGD (2 inputs, 6 outputs), and CGD (2 inputs, 12 outputs) architectures, respectively, illustrating how increasing configuration complexity is accompanied by additional mixing rings, longer mixing paths, and a larger internal fluidic volume. As the number of outputs increases, the total upstream path length and dead volume increase substantially, which contributes to greater sensitivity to hydraulic resistance mismatch and to the need for higher flow rates to achieve clear discretization. These estimates also indicate that reagent consumption can be reduced in practice through shorter operating times, reduced dead volume, shorter upstream flow paths, or the use of simpler configurations when maximum concentration resolution is not required.